NEOPLASIA
www.neoplasia.com

Volume 23 Number 11 Month 2021 pp. 1089–1100

Original Research

In vivo two-photon characterization of tumor-associated macrophages and microglia (TAM/M) and CX3CR1 during different steps of brain metastasis formation from lung cancer ☆, ☆☆

Wenlong Zhang [a,1]; Philipp Karschnia [b,c,1,*]; Iven-Alex von Mücke-Heim [a,1]; Matthias Mulazzani [a]; Xiaolan Zhou [a]; Jens Blobner [b,c]; Niklas Mueller [d]; Nico Teske [b,c]; Sertac Dede [a]; Tao Xu [a]; Niklas Thon [b,c]; Hellen Ishikawa-Ankerhold [e]; Andreas Straube [a]; Joerg-Christian Tonn [b,c]; Louisa von Baumgarten [a,b,c,*]

[a] Department of Neurology, Ludwig-Maximilians-University School of Medicine, Munich, Germany
[b] Department of Neurosurgery, Ludwig-Maximilians-University School of Medicine, Munich, Germany
[c] German Cancer Consortium (DKTK), Partner Site Munich, Germany
[d] Department of Medicine III, Ludwig-Maximilians-University School of Medicine, Munich, Germany
[e] Department of Medicine I, Ludwig-Maximilians-University School of Medicine, Munich, Germany

Abstract

Brain metastases frequently occur in lung cancer and dramatically limit prognosis of affected patients. The influence of tumor-associated macrophages and microglia (TAM/M) and their receptor CX3CR1 on different steps of brain metastasis formation from lung cancer is poorly characterized. We established a syngeneic orthotopic cerebral metastasis model in mice by combining a chronic cranial window with repetitive intravital 2-photon laser scanning microscopy. This allowed *in vivo* tracking of fluorescence-expressing tumor cells and TAM/M on a single-cell level over weeks. Intracarotid injection of red tdTomato-fluorescent Lewis lung carcinoma cell was performed in transgenic mice either proficient or deficient for CX3CR1. After intracarotid cell injection, intravascular tumor cells extravasated into the brain parenchyma and formed micro- and mature macrometastases. We observed potential phagocytosis of extravasated tumor cells by TAM/M. However, during later steps of metastasis formation, these anti-tumor effects diminished and were paralleled by TAM/M accumulation and activation. Although CX3CR1 deficiency resulted in a lower number of extravasated tumor cells, progression of these extravasated cells into micro metastases was more efficient. Overall, this resulted in a comparable number of mature macrometastases in CX3CR1-deficient and -proficient mice. Our findings indicate that unspecific inhibition of CX3CR1 might not be a suitable therapeutic option to prevent dissemination of lung cancer cells to the brain. Given the close

* Corresponding author.
E-mail addresses: P.Karschnia@med.uni-muenchen.de (P. Karschnia), Louisa.vonBaumgarten@med.uni-muenchen.de (L. von Baumgarten).

☆ Funding: P.K. acknowledges research grants from the Friedrich-Baur-Foundation, from the "Support Program for Research and Teaching" at the Ludwig-Maximilians-University Munich, from the "Society for Research and Science at the Medical Faculty of the LMU" at the Ludwig-Maximilians-University Munich, and from the "Familie Mehdorn"-Foundation. W.Z., X.Z., and T.X. acknowledge scholarship support from China Scholarship Council (CSC). I.vM. acknowledges support from the Else-Kröner-Fresenius Stiftung. M.M. acknowledges funding from the Friedrich-Baur-Foundation and an EFNS scientific fellowship. J.B. acknowledges research grants from the Munich Clinician Scientist Program "Else-Kröner-Fresenius Forschungskolleg" and of the Medical Faculty of the Ludwig-Maximilians-University Munich. N.T. acknowledges a research grant from the "Support Program for Research and Teaching" at the Ludwig-Maximilians-University Munich. H.I-A acknowledges the SFB 914 (project Z01). L.v.B. acknowledges support by the Else Kröner Fresenius Kolleg "Cancer Immunotherapy", "Deutsche Forschungsgemeinschaft" (DFG, German Research Foundation, SFB-TRR 338), research grants from the Advanced Munich Clinician Scientist Program and from Else Kröner Fresenius Foundation (grant #A265). L.v.B. and the whole 'AG for Experimental Neuro-Oncology' thankfully acknowledge the generous financial research support from Marlene and Dr. Dirk Ippen.

☆☆ Conflict of Interest: *Wenlong* Zhang - No disclosures, *Philipp Karschnia* - No disclosures., *Iven-Alex von Mücke-Heim* - No disclosures., *Matthias Mulazzani* - One-time member of a scientific advisory committee for Gilead., *Xiolan Zhou* - No disclosures., *Jens Blobner* - No disclosures., *Mueller* - No disclosures., *Nico Teske* - No disclosures., *Sertac Dede*- No disclosures., *Tao Xu* - No disclosures., *Niklas Thon* - No disclosures., *Hellen Ishikawa-Ankerhold* - No disclosures., *Andreas Straube* - No disclosures., *Joerg-Christian Tonn* - Research grants from Novocure and Munich Surgical Imaging; honoraria for lectures from CarThera; and Royalties from Springer Publisher Intl., *Louisa von Baumgarten* - No disclosures.

[1] The authors contributed equally to the manuscript.

Received 6 June 2021; received in revised form 5 August 2021; accepted 1 September 2021

https://doi.org/10.1016/j.neo.2021.09.001

interaction between TAM/M and tumor cells during metastasis formation, other therapeutic approaches targeting TAM/M function may warrant further evaluation. The herein established orthotopic mouse model may be a useful tool to evaluate such concepts *in vivo*.

Neoplasia (2021) 23, 1089–1100

Keywords: cerebral metastasis, lung cancer, macrophages, microglia, two-photon microscopy, CX3CR1

Introduction

Brain metastases arise through the dissemination of cells from an extracranial primary neoplasm to the brain microvasculature. 20% to 40% of patients with solid cancers develop brain metastases, and individuals with lung cancer are at particularly high risk [1]. Although recent immunotherapeutic advances improved outcome for systemic lung cancer [2], brain metastases from lung cancer still respond poorly to medical therapy and limit survival 3,4. Factors contributing to the formation of brain metastases are largely unknown, but might be of relevance for the identification of therapeutic strategies.

Metastases are compositions of neoplastic and non-neoplastic cells which all contribute to metastasis formation [5]. Tumor-associated macrophages and microglia (TAM/M) of peripheral or brain-intrinsic origin represent the majority of non-neoplastic cells in the tumor microenvironment. Once activated, TAM/M create an immunosuppressive niche which facilitates tumor cell extravasation and expansion [6]. Accordingly, TAM/M-density correlates with poor prognosis in malignancies inside and outside the central nervous system [7]; and TAM/M-inhibition was reported to decrease metastases in pancreatic cancer xenografts and hamper progression of patient-derived glioma xenografts [8,9]. Contrary, TAM/M may also exhibit anti-tumor properties in other brain tumors such as medulloblastoma via direct killing activity against tumor cells [10]. Thus, the role of TAM/M in brain cancer formation likely depends on the exact tumor-type, which remains to be specified for lung cancer metastases. Animal models for the cerebral dissemination of lung cancer cells have been successfully established. [11,12]. However, repetitive *in vivo*-visualization of lung cancer metastasis formation in the brain to study the interaction between tumor cells and TAM/M has not yet been reported.

TAM/M are regulated by a variety of signaling pathways including the C-X3-C motif chemokine receptor 1 (CX3CR1)/C-X3-C motif chemokine ligand 1 (CX3CL1)-axis [13]. Under physiologic conditions, mostly macrophages and microglia express CX3CR1. The ligand CX3CL1 is an abundantly expressed chemokine and can be found on tissues of epithelial origin including pulmonal tissue (and, thus, also lung cancer) [14]. Elevated CX3CL1-levels are associated with activation of immunosuppressive (potentially pro-tumorous) TAM/M [15], but also with increased infiltration of pro-inflammatory (potentially anti-tumorous) immune cells [16]. Whether the CX3CR1/CX3CL1-axis represents a therapeutic target in brain metastases from lung cancer remains therefore unclear.

We herein developed an orthotopic mouse model to study the formation of brain metastases after systemic dissemination of lung cancer cells. This model allowed the repetitive visualization of fluorescent cancer cells, TAM/M, and blood vessels using two-photon laser scanning microscopy through a chronic cranial window. Thereby, we were able to analyze *in vivo* the interaction of tumor cells with TAM/M during different steps of metastasis formation. To illustrate the role of the CX3CR1/CX3CL1-axis in brain metastases formation from lung cancer, we made use of CX3CR1 knock-out mice.

Materials and methods

Animals

Homozygous CX3CR1$^{GFP/GFP}$-mice (B6.129P-Cx3cr1t^{m1Litt}/J; JAX stock #005582) were purchased from The Jackson Laboratory. These mice have a green fluorescent protein (GFP)-sequence replacing the first 390 base pairs of the coding exon 2 within the CX3CR1-gene, thus enabling the visualization of CX3CR1-expressing TAM/M. Homozygous CX3CR1$^{GFP/GFP}$-mice were bred with C57BL/6J-mice to generate heterozygous CX3CR1$^{GFP/wt}$-mice. Whereas homozygous CX3CR1$^{GFP/GFP}$-mice are functional knock-outs for CX3CR1, heterozygous CX3CR1$^{GFP/wt}$-mice are characterized by proper function of CX3CR1 [17,18]. For cranial window implantation, female mice with an age of 8 to 12 weeks were used. Animals were housed 1 per cage and had *ad libitum* access to tap water and standard pellet food. All animal experiments were approved by the local governmental animal care committee, and were conducted in accordance with German legislation and NIH Guidelines (NIH Publication #85-23 Rev. 1985).

Cell lines

LL/2, a murine Lewis lung carcinoma cell line, was purchased from the European Collection of Authenticated Cell Cultures (ECACC). Cells were cultured in DMEM supplemented with 2mM glutamine and 10% FCS, and regularly tested for mycoplasma infection. To keep genetic drift at minimum, cells were maintained in culture for up to 3 months after thawing.

Retroviral transfection

A vector was generated by cloning a PCR-product containing the tdTomato-sequence (vector ptdTomato; #632531, TaKaRa Clontech) into the lentiviral expression vector pLVX-IRES-neo (LentiX-Bicistronic Expression System; #632181, TaKaRa Clontech) [19]. This lentiviral expression vector contains a resistance-sequence for G418-sulfate. The resulting nucleotide construct pLVX-tdTomato-IRES-Neo was verified by restriction enzyme digestion and direct sequencing.

LL/2-cells were transfected with pLVX-tdTomato-IRES-Neo using lipofection (Lipofectamine 3000; Thermo Fisher Scientific). Immediately after transfection, ^{tdt}LL/2-cells were cultured in selection medium containing G418-sulfate and Geneticin (#A2912; Biochrom). TdTomato-positive clones were further enriched using FACS sorting [19].

Cranial window preparation and intracarotid tumor cell injection

Chronic cranial window preparation has been previously described in detail (Figure. 1) [19-21]. Briefly, dexamethasone (2 mg/kg) and

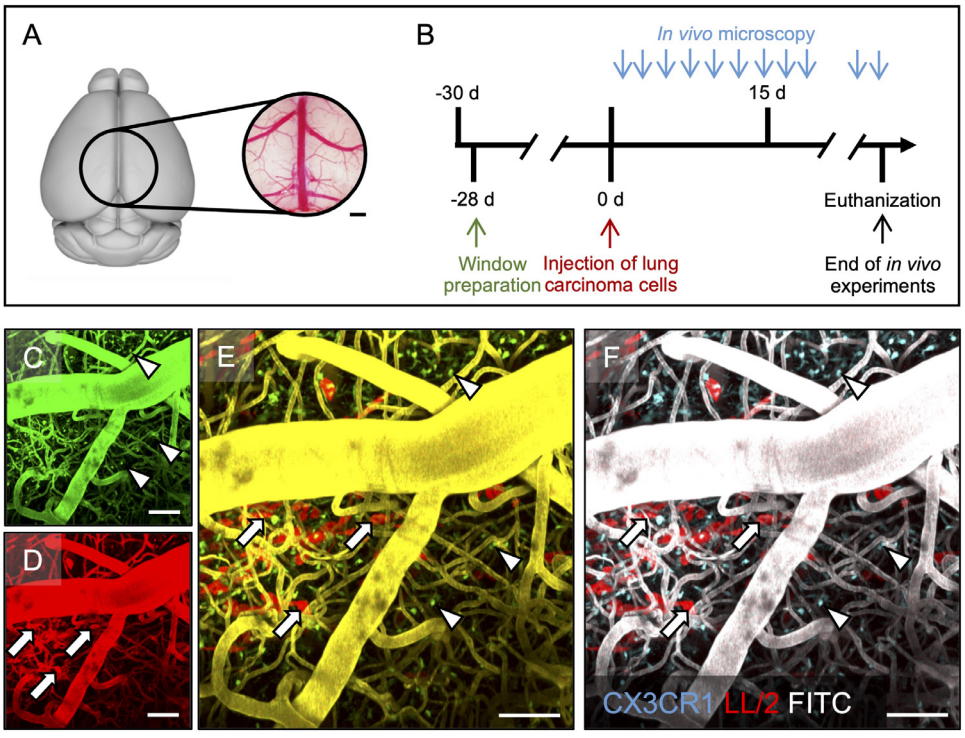

Fig. 1. Experimental protocol and post-hoc image processing.
A: Position and dimensions of the cranial window (circle; diameter 5.5 mm) over the mouse brain. The panel was created with the 3dBAR plugin of the Scalable Brain Atlas (Bakker *et al.* in Neuroinformatics, 2015). Scale bar: 0.5 mm. B: Timeline on of the experimental design. C-F: Post-hoc image processing merging channels from *in vivo*-microscopy (C, D) into resulting false-colour images (E, F). CX3CR1-positive tumor-associated macrophages and microglia (TAM/M; arrowheads) can almost exclusively be found in the green channel (C), whereas red fluorescent ^{tdt}LL/2 tumor cells (arrows) are only seen in the red channel (D). Given the signal overlap from intravascular FITC-dextran in the green and the red channel, yellow vessels are displayed after merging whereas the colour of TAM/M and tumor cells remains the same (E). For better visualization, vessels colour was changed to white, TAM/M colour to cyan, and tumor cells remained red (F). Depth from brain surface: 1-300 µm. Scale bars: 50 µm.

cefotaxime (250mg/kg) were preoperatively administered. A circular part of the cranium (diameter: 5.5mm) was removed and the dura mater was carefully separated from the leptomeninges to achieve optimal image resolution (Figure. 1A). The brain surface remained covered with saline, and a round cover class (diameter: 6.0mm) was firmly attached to the bone. A custom-made ring (diameter: 8.00mm) was glued to the skull to facilitate head positioning during imaging. To ensure postoperative analgesia, buprenorphine (0.1mg/kg; q8h) was injected for 2 postoperative days. The animals were allowed a postoperative recovery time of 28 days to prevent postoperative microglia activation or alterations of the microcirculation (Figure. 1B).

To simulate cerebral tumor cell dissemination, we injected ^{tdt}LL/2-cells into the carotid artery [22]. For that purpose, the right common carotid artery, internal carotid artery, and external carotid artery were exposed. The proximal common carotid artery and the proximal external carotid artery were ligated to ensure anterograde flow of the tumor cells into the brain. 7.5×10^5 ^{tdt}LL/2-cells in 150µl PBS were then injected into the common carotid artery over 5 minutes; and the common carotid artery distal from the injection site was also ligated to prevent bleeding or tumor cell regurgitation. Wound was closed and analgesia was provided.

Two-photon laser scanning microscopy and image acquisition

Metastasis formation was followed by *in vivo*-microscopy (Figure 1B). For this purpose, a TrimScope multiphoton microscopy platform (LaVision Biotech TrimScope I) equipped with a MaiTai-laser (wavelength 690-1040nm; Spectra Physics, Newport) and a 20-times water immersion objective (numerical aperture 0.95; XLUMPlanFl, Olympus) was used. 6 standardized regions of interest (ROIs) per animal were longitudinally assessed with a x20 objective. Anesthesia during microscopy was established with 1% to 2% isoflurane in oxygen adjusted to the breathing rate; and the mice's head was fixated in a custom-made holding device. Subsequently, 0.2mL fluorescein isothiocyanate (FITC)-dextran (10mg/mL, 2 MDa molecular mass; Sigma-Aldrich) were injected into the tail vein for intravascular plasma staining. Cortical vessels were identified by the fluorescent signal of FITC-dextran and served as landmarks to retrieve the same ROIs during repetitive imaging. Image stacks with x/y/z-dimensions of $450 \times 450 \times 300$ μm were acquired at a wavelength of 920nm. Imaging started at the brain surface (as defined by detection of the arachnoid fibers using second harmonic imaging) and recordings were made every 2µm. Image resolution was set at 1024×1024 pixels.

Image analysis

For image analysis, Imaris v8.2 (Bitplane AG) and ImageJ/Fiji (NIH) were used. Raters were blinded to group allocation until analyses were completed. Tumor cells were identified using their intrinsic red fluorescence and were followed through the different steps of metastasis formation [21]. The intratumoral density (in 10^4/mm^3) of green fluorescent TAM/M was determined within an area of $100 \times 10 \times 40$ µm around the center of a

metastasis. The average cell body volume (in μm^3/cell) of all TAM/M within the respective area as an indirect marker of cellular activation was calculated after semi-automatic cell delineation. For display purposes, 2-dimensional images were generated using maximum intensity projections for merged channels.

Study design

Tumor cells were intracarotidly injected into both CX3CR1$^{GFP/wt}$- and CX3CR1$^{GFP/GFP}$-mice (n=8 each) to analyze the role of the CX3CR1/CX3CL1-axis on the formation of brain metastases of lung cancer. In addition, CX3CR1$^{GFP/wt}$- and CX3CR1$^{GFP/GFP}$-mice in which cranial window preparation but no intracarotid (tumor cell) injection was performed served as controls (n=3 each). *In vivo*-microscopy was performed 1 day after tumor cell injection and then every other day until termination criteria (including neurologic symptoms attributed to tumor growth or tumor diameter >3mm) were met. At the end of the *in vivo*-experiments, animals were sacrificed by intracardiac injection of PBS followed by PFA 4%, and the brains were excised.

Immunohistochemical analysis

After excision, brains were stored in PFA 4% for at least 2 hours. Subsequently, the water was removed from the samples by incubation in ascending sucrose series until equilibration was reached. Samples were transferred to -20°C for 24 hours and eventually into liquid nitrogen. Finally, brains were cut into 15µm-thick sections.

Sections were stained with a polyclonal goat-anti-mouse antibody against Iba1 (#NB100-1028; 1:100, Novus Biologicals) to detect TAM/M, and with a polyclonal rabbit-anti-DS-red antibody (#632496; 1:200, Clontech) to highlight the tdTomato-signal of tumor cells. The endogenously expressed GFP-signal of CX3CR1-positive TAM/M could be detected without further staining. As secondary antibodies, a donkey-anti-goat AlexaFluor®-647 antibody (#A-21447; 1:100, Thermo Fisher Scientific), and a donkey-anti-rabbit AlexaFluor®−594 antibody (#A21207; 1:100, Invitrogen) were used. The sections were placed in a humidified incubation box and incubated overnight at 4°C with the primary antibody. The labelling with the respective secondary antibody was performed at room temperature for 1h. Cell nuclei were stained with DAPI (#236276; 1:1000, Roche). Sections were assessed using a Zeiss AxioImager.M2 upright-microscope (Carl Zeiss Microscopy). To immunohistochemically quantify the TAM/M-signal, we determined the fluorescence signal intensity (per area) of the TAM/M-markers GFP (representing the CX3CR1-signal) and Iba1 within the tumor (manually delineated), peritumoral (six ROIs per 200 × 200 µm), and contralateral (area and localization corresponding to the analyzed tumor area) using Zen Lite software package (version 2.3; Carl Zeiss Microscopy).

Statistics

Normal distribution and equal variance of data was tested using the D' Agostino-Pearson omnibus normality-test. Differences between CX3CR1$^{GFP/wt}$-mice, CX3CR1$^{GFP/GFP}$-mice, and respective controls or between different time points within groups were analyzed by the student's *t*-test (parametric data) or by the Mann-Whitney U-test (non-parametric data). All values are expressed as mean ± standard error of the mean (SEM), if not indicated otherwise. Relationships between two categorical variables were analyzed using Fisher's exact test. Statistical analyses were performed using Prism statistical software (Prism 7.02; GraphPad Software). The significance level was set at $P \leq 0.05$. Post-hoc correction using the False Discovery Rate was performed.

Results

Development of a robust mouse model for in vivo-imaging of tumor metastasis

Microsurgical implementation of a chronic cranial window was well tolerated and enabled repetitive visualization of the mouse brain at the exact same coordinates *in vivo* using two-photon laser-scanning-microscopy. After cranial window preparation, TAM/M-density constantly decreased during the recovery time of 28 days prior to intracarotid tumor cell injection (relative density reduction compared day 4: 9% on day 14, 20% on day 21, 36% on day 28; n=3). This finding may suggest recovery from surgical trauma. After intracarotid injection of ^{tdt}LL/2, both CX3CR1$^{GFP/wt}$-mice and CX3CR1$^{GFP/GFP}$-mice developed numerous solid intracerebral tumors across the ipsilateral cerebral hemisphere. All mice (n=8 per group) had tumor take after intracarotid tumor cell injection, and window quality as well as fluorescence intensity remained high until end of the *in vivo*-experiments.

Tumor cells were identified based upon their red fluorescence signal, and TAM/M were detected based upon their green fluorescence signal. Intravascular plasma staining was facilitated using green fluorescent FITC-dextran. Given the signal overlap of GFP-positive TAM/M and intravascular FITC-dextran during *in vivo*-microscopy at a wavelength of 920 nm (*Supplementary Table 1*), post-hoc image processing was established (Figure 1C-F). The strong signal of FITC-dextran was detected in both the green as well as in the red channels during microscopy, whereas TAM/M and ^{tdt}LL/2 were almost exclusively seen in their respective channels with low cross-talk between the channels. We therefore merged the green with the red channel (where tumor cells and vessels structures could be identified) and applied further color processing (overlay, followed by adjusting contrast), resulting in a pseudo-color image in which CX3CR1-positive TAM/M were re-colored with cyan colors, ^{tdt}LL/2 was represented by red color, and vessels stained by FITC-dextran were visible by gray color.

Different steps of brain metastasis formation

In both CX3CR1$^{GFP/wt}$-mice and CX3CR1$^{GFP/GFP}$-mice, we found ^{tdt}LL/2 cells within the cerebral vasculature after tumor cell injection. Intravascular arrest of these red fluorescent tumor cells was displayed as early as day 1 after tumor cell injection (in CX3CR1$^{GFP/wt}$-mice: 107 intravascularly arrested cells; CX3CR1$^{GFP/GFP}$-mice: 137 intravascularly arrested cells), followed by extravasation in 29-43% of the intravascularly detected cells (Figure 2). Median diameter of the vessels the cells were extravasating from was 8.0±4.0 µm, median tumor cell diameter was 8.0±0.3 µm, and cell-vessel-diameter ratio was therefore 1:1 as previously described [21]. Extravasation of ^{tdt}LL/2 was frequently accompanied by migration of TAM/M towards the tumor cells.

Formation of metastases was highly inefficient, and 51-80% of extravasated cells did not proliferate within the following days and perished (CX3CR1$^{GFP/wt}$-mice: 37/46 cells; CX3CR1$^{GFP/GFP}$-mice: 20/39 cells). In selected cells which eventually perished, we were able to observe incorporation of the tumor cells into the TAM/M (Figure 2A-D). In this context we were able to co-localize red florescent signal to TAM/M, which might be indicative of ^{tdt}LL/2 phagocytosis. When the red fluorescence within TAM/M diminished, many TAM/M remained at the place of former tumor extravasation. Importantly, this observation was made both in CX3CR1$^{GFP/wt}$ and CX3CR1$^{GFP/GFP}$-mice (Figure 2E-H).

In turn, 20-49% of ^{tdt}LL/2 (CX3CR1$^{GFP/wt}$-mice: 9/46 extravasated cells; CX3CR1$^{GFP/GFP}$-mice: 19/39 cells) which successfully extravasated into the surrounding brain parenchyma also proliferated exponentially within the following days (Figure 3). This process resulted in the formation of micrometastases (defined as 4-50 cells/ROI) within 3 to 7 days in CX3CR1$^{GFP/wt}$-mice (Figure 3A-D) and CX3CR1$^{GFP/GFP}$-mice (Figure 3E-

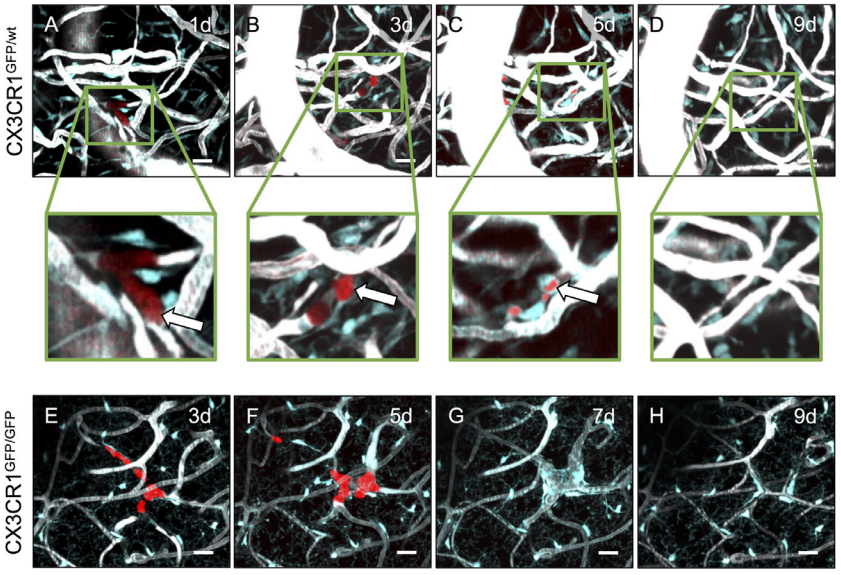

Fig. 2. Anti-tumor effects of TAM/M against extravasated tumor cells.
A-H: Representative maximum intensity projections of extravasating tumor cells in CX3CR1-proficient (A-D) and -deficient (E-H) mice on days 1, 3, 5, 7, and 9 after intracarotid tumor cell injection. The same regions of interest were followed over time in each mouse (for reference, e.g. note the prominent vein structure on the left side of Figures 2A-D), and successfully extravasated tumor cells can be detected (arrows). TAM/M migrate to the site and incorporate the tumor cells (inlay in A-D), which may indicate phagocytosis. Depth from brain surface: A-D: 14-30 µm; E-H: 100-150 µm. Scale bars: 50 µm.

H) [21]. Although cases of spontaneous micrometastasis regression were observed (*Supplementary Figure 1*), 56% to 84% of micrometastases evolved into actively growing macrometastases (defined as >50 cells/ROI or maximal tumor diameter >50 µm) within 5 to 9 days after tumor cell injection. No observations suggestive of phagocytosis were made after macrometastases have formed.

After extravasation of tumor cells, early metastatic growth was usually located in a perivascular localization at vascular branch points, which might be due to rheological blood flow properties. Formation of new microvessels, but also changes in vessel morphology such as elongation or increased tortuosity were seen (*Supplementary Figure 2*). There were no striking differences regarding vascular morphology between $CX3CR1^{GFP/wt}$- and $CX3CR1^{GFP/GFP}$-mice.

Progressive TAM/M-accumulation and -activation during metastasis formation

Our analyses showed that tumor growth in this animal model was paralleled by an intra- and peritumoral accumulation of TAM/M in both $CX3CR1^{GFP/wt}$-mice and $CX3CR1^{GFP/GFP}$-mice (Figure 3I-L). As soon as single tumor cells extravasated into the surrounding brain tissue, we detected a small but significant increase in TAM/M-density which further progressed during formation of micro- and macrometastasis. Macrometastases were associated with the highest TAM/M-numbers. TAM/M-accumulation was associated with a constant increase in cell body volume as an indirect sign of TAM/M-activation [23]. The highest TAM/M cell body volumes were found in macrometastases. Importantly, detailed analyses of spontaneously regressed micrometastases revealed that TAM/M-density and volume decreased again during tumor regression. However, in the case of tumor regression neither TAM/M-density nor -volume reached levels of healthy controls. TAM/M of perivascular origin seemed to be recruited during early metastatic growth (*Supplementary Figure 2*), whereas during later stages of tumor growth TAM/M-migration from the parenchyma appeared increased.

Tumor growth and TAM/M in $CX3CR1^{GFP/wt}$-mice and $CX3CR1^{GFP/GFP}$-mice

We tracked the initially intravascularly migrated tumor cells in $CX3CR1^{GFP/wt}$- and $CX3CR1^{GFP/GFP}$-mice over weeks to characterize the role of CX3CR1 on the different steps of metastasis formation (extravasation into the brain tissue; proliferation to micrometastasis; further growth into macrometastasis) (Figure 4). We successfully visualized >100 intravascular tumor cells one day after intracarotid injection in both $CX3CR1^{GFP/wt}$-and $CX3CR1^{GFP/GFP}$-mice (Figure 4A). Extravasation of the detected tumor cells into the surrounding brain parenchyma was successful in >40% of the cells in $CX3CR1^{GFP/wt}$-mice but only in about 30% in $CX3CR1^{GFP/GFP}$-mice. In contrast, more tumor cells formed micrometastases in $CX3CR1^{GFP/GFP}$ (49%, 9/39 of extravasated cells) compared to $CX3CR1^{GFP/wt}$-mice (20%, 9/46 of extravasated cells) after extravasation took place. After formation of micrometastases, the majority ($CX3CR1^{GFP/GFP}$: 16/19 of micrometastases, 84%; $CX3CR1^{GFP/wt}$: 5/9 of micrometastases, 56%) progressed to exponentially growing macrometastases, and there was no statistical difference in the rate of micrometastases progression to macrometastases. Thus, the lower extravasation rate in $CX3CR1^{GFP/GFP}$-mice was functionally compensated by an increased micrometastasis formation; ultimately resulting in a similar number of macrometastasis in $CX3CR1^{GFP/GFP}$- and $CX3CR1^{GFP/wt}$-mice. Accordingly, survival was between 9-19 days after tumor cell injection in both $CX3CR1^{GFP/wt}$-mice and $CX3CR1^{GFP/GFP}$-mice ($CX3CR1^{GFP/wt}$-mice: 16±1 days *versus* $CX3CR1^{GFP/GFP}$-mice: 14±1 days).

We also assessed differences in TAM/M between the groups. Both groups exhibited a similar density and cell body volume of TAM/M after cranial window preparation (Figure 4B, C). After intracarotid tumor cell injection, differences in TAM/M were observed: higher numbers of intratumoral TAM/M were seen in $CX3CR1^{GFP/wt}$-mice as soon as single tumor cells extravasated, and this difference was maintained in macrometastases (Figure 4D). The lower TAM/M-density in $CX3CR1^{GFP/GFP}$-mice was accompanied by a compensatory increase in cell body volume compared

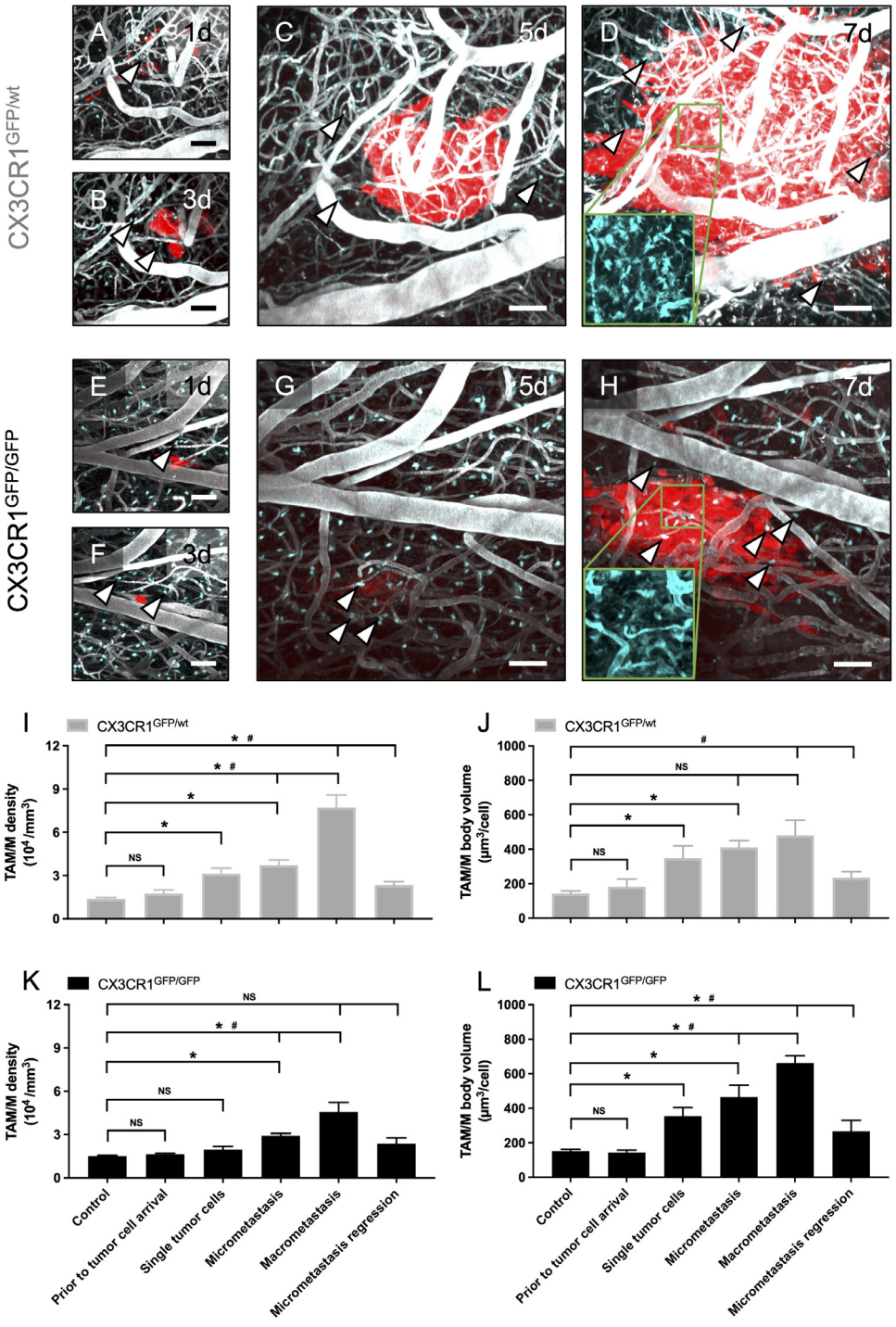

Fig. 3. Successful formation of macrometastases paralleled by TAM/M accumulation and activation.
A-H: Representative maximum intensity projection of tumor cells which successfully progressed to macrometastases in CX3CR1-proficient (A-D) and -deficient (E-H) mice on days 1, 3, 5, and 7 after intracarotid tumor cell injection. Metastatic growth was associated with an intra- and peritumoral accumulation of TAM/M (arrowheads). Note that higher numbers of TAM/M can be detected in macrometastases from CX3CR1-proficient mice (inlay in D) compared to CX3CR1-deficient mice (inlay in H). Inlays in D and H represent false-colour images of the unmerged green channel only. Depth from brain surface: 0-200 µm. Scale bars: A, B, E, F: 50 µm. C, D, G, H: 33 µm. I-L: TAM/M density (I, K; 10^4/mm^3) and TAM/M body volume (J, L; µm^3/cell) within an area of 100 × 100 × 40 µm around the center of a metastasis in CX3CR1-proficient (I, J; n = 8) and CX3CR1-deficient (K, L; n = 8) mice, as assessed by two-photon laser scanning microscopy. TAM/M were characterized for each metastasis displayed in Figure 4A whenever possible. Means ± SEM. NS: not significant. $^{*}P \leq 0.05$ *vs.* control. $^{\#}P \leq 0.05$ *vs.* preceding column.

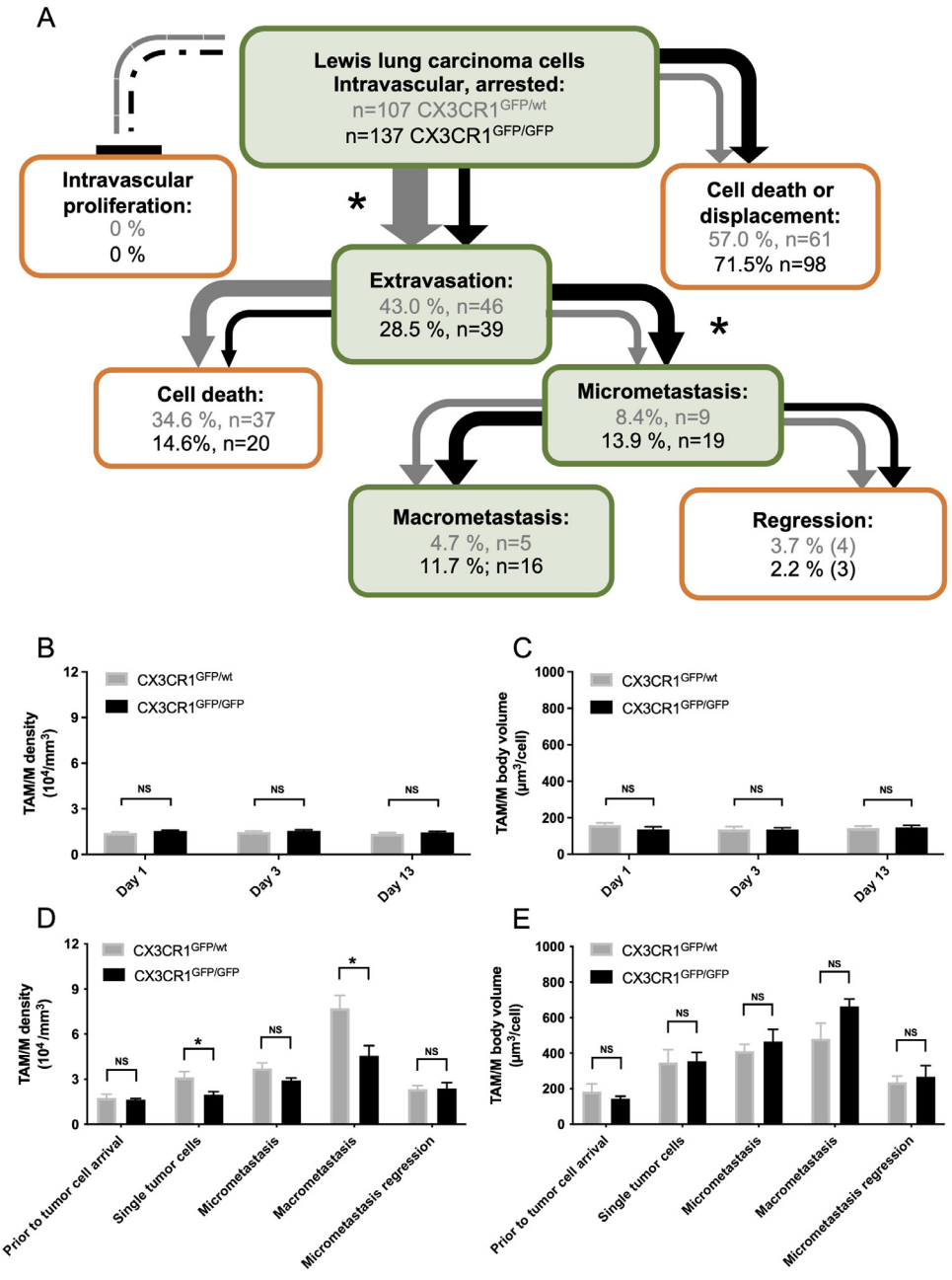

Fig. 4. Influence of CX3CR1 on metastasis formation and TAM/M.
A: Tracking of individual tumor cells across the different steps of metastasis formation including intravascular arrest, extravasation into the brain parenchyma, formation of micrometastases, and progression to macrometastases. Data are given for CX3CR1-proficient mice (grey; n = 8) and CX3CR1-deficient mice (black; n = 8). $^{*}P \leq 0.05$ (compared between the two groups). B-E: Comparison of TAM/M density (B, D; 10^4/mm^3) and TAM/M body volume (C, E; µm^3/cell) 28 days after cranial window preparation (B, C) and after intracarotid tumor cell injection (D, E), as assessed by two-photon laser scanning microscopy. Data are indicated for CX3CR1-proficient mice (grey; n = 8) and CX3CR1-deficient mice (black; n = 8), and partly represent data previously shown in Figure 3I-L. Means ± SEM. NS: not significant. $^{*}P \leq 0.05$ (compared between the two groups).

to CX3CR1$^{GFP/wt}$-mice. This phenomenon was most prominent in macrometastases but absent early at single tumor cell arrival (Figure 4E).

Growth patterns of macrometastases

By detection of the inherent fluorescent signal of the tumor cells, metastases were found in all mice at the end of the *in vivo*-experiments (Figure 5). Detailed immunohistochemical analyses revealed four growth patterns of metastases, which were not evident during *in vivo*-microscopy: (I) leptomeningeal dissemination of tumor cells, (II) metastases to the choroid plexus, (III) vascular co-option of parenchymal vessels, and (IV) nodular metastases within the brain parenchyma (Figure 5A-D). Leptomeningeal dissemination was the most commonly found growth pattern (CX3CR1$^{GFP/wt}$: 8/8 mice, 100%; CX3CR1$^{GFP/GFP}$: 7/7 mice, 100%), followed by choroid plexus metastases and vascular co-option (CX3CR1$^{GFP/wt}$: 5/8 mice, 63% each; CX3CR1$^{GFP/GFP}$: 6/7 mice, 86% each).

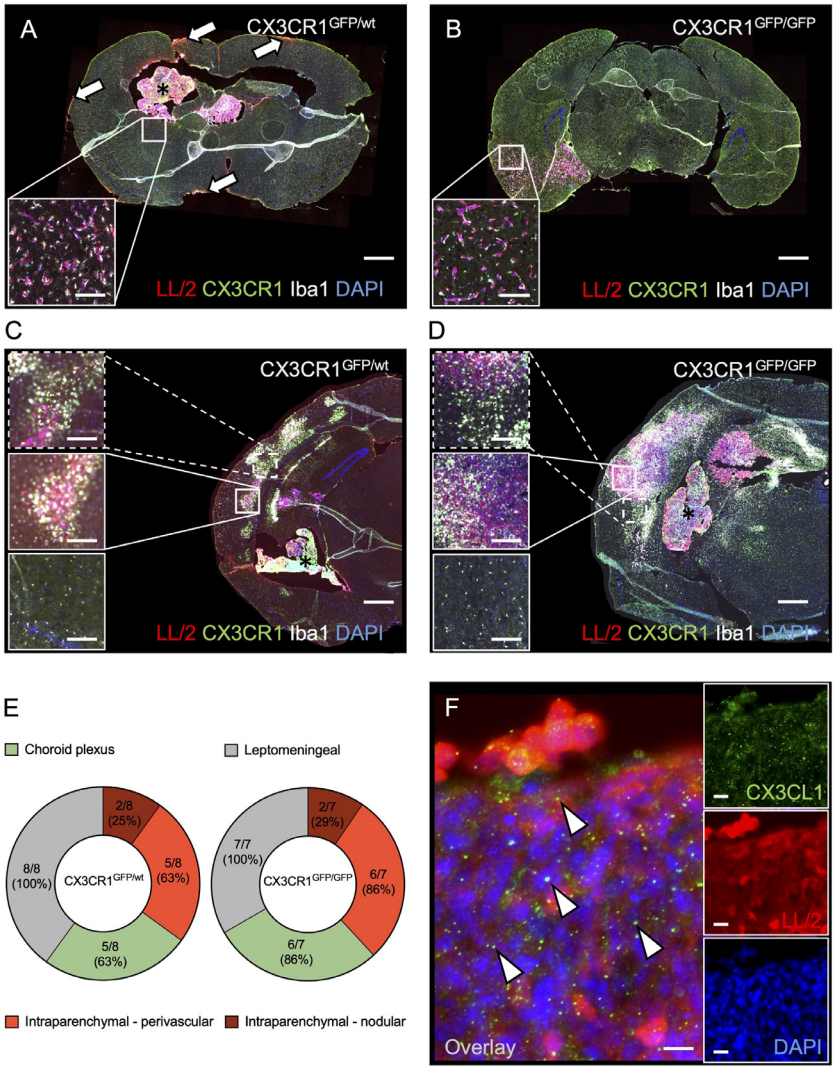

Fig. 5. Immunohistochemical characterization of metastasis formation and TAM/M.
A-D: Histological sections of brains from CX3CR1$^{GFP/wt}$ mice (A, C) and CX3CR1$^{GFP/GFP}$ mice (B, D) excised between day 15-18 after intracarotid injection of ^{tdt}LL/2 tumor cells. Sections were stained with an antibody against TdTomato for the detection of tumor cells (red), an antibody against Iba1 to confirm detection of TAM/M (white), and with DAPI to identify cell nuclei (blue). The endogenously expressed GFP-signal of CX3CR1-positive TAM/M (green) could be detected without further staining. Four different growth patterns were observed: (I) leptomeningeal dissemination of tumor cells (arrowheads in A), (II) metastases to the choroid plexus (asterisks in A, C, D), (III) vascular co-option of parenchymal vessels (inlays in A, B), (IV) nodular metastases within the brain parenchyma (inlays in C, D). Note that particularly nodular intraparenchymal metastases are accompanied by accumulation of CX3CR1-/Iba1 double-positive TAM/M within the tumor (middle inlay in C, D) as well as peritumoral (upper inlay in C, D) when compared to healthy contralateral brain tissue (lower inlay in C, D). Please further note, that the inlay in Figure 5A does not refer to the exact same slice, but to a sampling point in the same brain and area about 100 µm distant from the displayed slice. However, the given slice has been selected for graphical purposes. Scale bars: A, B: 1 mm (inlays: 140 µm). B, C: 500 µm (inlays: 155 µm). E: Frequency of metastasis growth patterns in CX3CR1$^{GFP/wt}$ mice (left; n = 8) and CX3CR1$^{GFP/GFP}$ mice (right; n = 7). The number of brains with the respective growth pattern were counted in each group, and donut charts indicate the relative frequency of the growth patterns to each other. Also, absolute numbers are given. F: Sections of ^{tdt}LL/2 tumor cells stained with an antibody against TdTomato to enhance the tumor cell signal (red), an antibody against CX3CL1 to identify the ligand of CX3CR1 (arrowheads; green), and DAPI to detect cell nuclei. The large image represents a merge of the inlays. Scale bar: 12 µm (inlays: 18 µm).

Nodular parenchymal metastases were least commonly seen (CX3CR1$^{GFP/wt}$: 2/8 mice, 25%; CX3CR1$^{GFP/GFP}$: 2/7 mice, 29%). There was no association of a particular growth pattern with CX3CR1$^{GFP/GFP}$-mice or CX3CR1$^{GFP/wt}$-mice (Figure 5E). Whereas some leptomeningeal dissemination of tumor cells was also found on the left hemisphere, intraparenchymal metastases were exclusively found within the right hemisphere (ipsilateral to the intracarotid injection site). Moreover, immunohistochemical detection of CX3CL1 confirmed the presence of the CX3CR1-ligand within the tumor tissue, whereas no substantial CX3CL1-expression was detected in the normal brain parenchyma (Figure 5F). Notably, further immunohistochemical phenotyping of TAM/M was not successful in our hands.

Co-detection of CX3CR1 and Iba1 confirmed the presence of intra- and peritumoral TAM/M, and TAM/M-infiltration was particularly pronounced in nodular intraparenchymal metastases. We further quantified the fluorescence signal intensity (per area) of the TAM/M-markers GFP (representing the CX3CR1 signal) and Iba1 within the tumor, peritumoral,

and in the healthy contralateral hemisphere. In CX3CR1$^{GFP/wt}$-mice, intratumoral and peritumoral signal intensity was increased compared to healthy tissue (GFP signal: 132% intratumoral, 109% peritumoral; Iba1 signal: 157% intratumoral, 115% peritumoral). In contrast, intratumoral signal in CX3CR1$^{GFP/GFP}$-mice was less pronounced and peritumoral signal was not substantially increased (GFP signal: 119% intratumoral, 96% peritumoral; Iba1 signal: 123% intratumoral, 97% peritumoral).

Discussion

Lung cancer represents the most frequently encountered solid tumor disseminating to the brain [1,4]. The role of TAM/M and CX3CR1 in the pathogenesis of brain metastases from lung cancer is poorly understood. We herein combined a murine model of cerebral tumor cell dissemination with repetitive *in vivo*-imaging which offers the exciting opportunity to assess metastatic tumor growth and the surrounding TAM/M over weeks. Anti-tumor effects of TAM/M were observed early after extravasation of single tumor cells. In contrast, TAM/M were morphologically activated in growing metastases and accumulated within intra- and peritumoral macrometastatic tissue. In case of spontaneous regression, neither TAM/M density nor volume reached physiologic levels indicating glial scarring. Our data therefore point towards a dynamic and close interaction of TAM/M and metastasis formation.

Functional CX3CR1 knock-out resulted in fewer tumor cells extravasating into the brain tissue. Furthermore, the intratumoral density of TAM/M during metastasis formation was significantly lower in CX3CR1 knock-out mice. This was paralleled, however, by a more successful rate of micrometastasis formation resulting in a comparable number of macrometastases in mice with and without functional CX3CR1 knock-out.

TAM/M constitute the majority of non-neoplastic cells in primary and secondary brain tumors [24]. Recent in-depth characterizations of cerebral metastases from lung cancer have shown that about 10% of TAM/M represent macrophages of peripheral origin in early metastases, and this number increases to 20% in large metastases [25]. Activation classes of TAM/M include the pro-inflammatory, anti-tumor M1-like and the anti-inflammatory, pro-tumor M2-like phenotype 26,27]. These phenotypes represent the extreme ends of the TAM/M polarization spectrum [28]. We observed potential phagocytosis of tumor cells by TAM/M shortly after intracarotid injection as previously also described by others using *in vivo*- and *ex vivo*-approaches 29,30], but also found extensive TAM/M-accumulation in actively growing metastases. A more detailed analyses found morphologic correlates of TAM/M-activation in macrometastases characterized by increased cell body volumes but failed to detect such morphological activation in TAM/M surrounding single tumor cells after extravasation. An increase in TAM/M body volume has been previously associated with M2-like polarization of TAM/M in a murine model of cerebral melanoma metastasis [31]. Vice versa, a murine glioblastoma model recently demonstrated that detection of tumor cell phagocytosis by TAM/M was restricted to M1-like polarized TAM/M [29,32]. In line with these findings, our observations of anti-tumor effects during early steps and accumulation of morphologically activated TAM/M during later steps of metastasis formation may reflect a progressive polarization from the anti-tumor M1-like towards the pro-tumor M2-like phenotype. However, some uncertainties remain given that immunohistochemical TAM/M phenotyping was not successful in our hands. As such, our model therefore did also not allow to distinguish between CX3CR1-positive TAM/M derived from the brain *per se* from such of peripheral origin.

Given the controversial data regarding the CX3CR1/CX3CL1-axis in the formation of brain metastases 33,34], we made use of a transgenic mouse line which allowed us to compare the effects of CX3CR1 knock-out on the metastatic cascade [21]. Our analysis showed that migration of intravascular tumor cells across the blood-brain barrier into the cerebral parenchyma and metastatic TAM/M-infiltration was impaired in CX3CR1 knock-out mice. In the healthy brain, CX3CR1 is mainly found on microglia and meningeal macrophages [35]. Its ligand CX3CL1 is not only expressed by lung cancer cells as immunohistochemically confirmed in our present study, but has also been described on astrocytes and endothelial cells inside as well as outside the brain [36,37]. This expression pattern may suggest involvement of the CX3CR1/CX3CL1-axis in the regulation of blood-brain barrier integrity and TAM/M-infiltration (the exact downstream pathways remain elusive, but may potentially involve the p38-MAPK signaling-pathway) [18]. Accordingly, lack of CX3CR1 has been described to protect the brain against viral invasion in an immunocompetent mouse model [38]. In turn, increased serum levels of cancer-derived CX3CL1 were associated with cerebral tumor dissemination in breast cancer patients [39]. CX3CL1 expression of tumor tissue may therefore induce tumor cell extravasation as well as metastatic TAM/M-infiltration, and absence of CX3CR1 may hamper migration of lung tumor cells into the brain.

On the other hand, we observed a higher rate of extravasated tumor cells progressing into micrometastases in CX3CR1-deficient mice. This was paralleled by a lower number of intra- and peritumoral TAM/M. Given that TAM/M were morphologically not activated as per *in vivo*-microscopy during these early steps of metastasis formation, it might be speculated that these TAM/M correspond to an anti-tumor M1-like rather than a pro-tumor M2-like phenotype. During later steps of metastasis formation, lower TAM/M numbers (detected by *in vivo*-microscopy and immunohistochemistry) in CX3CR1-deficient mice appeared to be compensated by a higher fraction of M2-like polarized TAM/M as indicated by larger cell body volumes in CX3CR1 knock-out mice. Thus, the progression of micrometastases to mature macrometastases was similar in mice with and without CX3CR1 knock-out. We hypothesize that the lower migration efficiency of tumor cells in CX3CR1 knock-out mice was counterbalanced by the increased micrometastases rate which eventually gave rise to an overall comparable number of macrometastases and survival between both groups. Although our study does therefore not support the theory that ubiquitous CX3CR1-blockade is beneficial in preventing brain metastases from lung cancer, selective CX3CR1-inhibition at the blood-brain barrier interface might be promising to suppress tumor cell migration into the CNS. Also, functional reprogramming of TAM/M rather than exclusive CX3CR1-depletion could represent a therapeutic avenue [9,40].

The *in vivo*-formation of brain metastasis was assessed in the cranial window model using two-photon laser scanning-microscopy. In contrast to conventional histological methods, this technique allows for repetitive analysis of tumor cells and TAM/M at single cell resolution [41,42]. Thus, we were able to reliably visualize brain metastasis growth. We herein often also observed unsuccessful steps of brain metastasis formation (e.g., tumor cell death or micrometastasis regression). Metastatic growth requires induction of angiogenesis, brain invasion via perivascular pathways, and adaption of tumor cells to brain-specific pathways [43]. Inability to induce such steps (e.g., due to an insufficient molecular profile of tumor cells) [44] may result in insufficient metastatic growth or regression.

We combined our *in vivo*-imaging approach with the intracarotid tumor cell injection which bears several major advantages including that (I) no further manipulation at the side of the cranial window is necessary which may result in artificial immune cell activation; (II) the injection technique mimics tumor cells dissemination across the blood-brain barrier starting from a peripheral, single-cell level; (III) metastases reliably form in the ipsilateral brain with no extra-axial metastases confounding survival and limiting the time for *in vivo*-imaging (although we cannot exclude formation of asymptomatic metastases outside of the brain). We found excellent imaging quality and robust orthotopic tumor growth in our animal model over the course of several weeks. Immunohistochemical analyses of excised brains revealed distinct metastatic growth patterns which have been previously described for human brain metastases, and may further confirm

the translational value of our model [45]. We did not find evidence that CX3CR1-deficiency was accompanied by a particular growth pattern, and also human studies did not find an association of growth patterns with a specific primary tumor type [45].

We only used female mice, given that sex-specific differences in microglia susceptibility to neuroinflammation have been described [46], and we aimed to exclude any sex-based differences between the groups. Cautionary, we cannot fully exclude some minor TAM/M-activation due to the cranial window preparation even though a recovery time of 28 days was maintained prior to tumor cell injection. Microglial activation and astrogliosis after cranial window preparation were shown to be transient and typically resolve after 14-21 days [47,48].

Although prior studies found no differences between $CX3CR1^{GFP/wt}$- and $CX3CR1^{wt/wt}$-mice regarding growth of primary brain tumors [18], we cannot comment on whether this would indeed also hold true for metastatic growth in our model given that differences regarding the microglial transcriptome have been described [49]. Also, future studies may want to consider using FITC-dextran with lower molecular weights to reliably detect blood-brain-barrier disruptions (which, however, would potentially limit visualization of single tumor cells or TAM/M due to extravasation of FITC-dextran).

Collectively, our study demonstrates the anti-tumor effects of TAM/M during early steps and the accumulation as well as activation of TAM/M during later steps of cerebral metastasis formation from lung cancer. Given the complex involvement of CX3CR1 in the metastatic cascade, unspecific CX3CR1-inhibition may not be a relevant therapeutic option to prevent dissemination of lung cancer cells to the brain unless the progression from micro- to macrometastases could be blocked efficiently by another yet to be defined intervention. Considering the high incidence and mortality of cerebral metastases from lung cancer, novel therapeutic strategies are urgently warranted. The herein established orthotopic mouse model may be a useful tool to evaluate such therapeutic concepts.

Author contributions

Wenlong Zhang - Data curation; Formal analysis; Investigation; Visualization; Roles/Writing - original draft; Writing - review & editing.

Philipp Karschnia - Formal analysis; Funding acquisition; Validation; Visualization; Roles/Writing - original draft; Writing - review & editing.

Iven-Alex von Mücke-Heim - Data curation; Formal analysis; Investigation; Validation; Visualization; Roles/Writing - original draft; Writing - review & editing.

Matthias Mulazzani - Formal analysis; Investigation; Writing - review & editing.

Xiolan Zhou - Formal analysis; Investigation; Writing - review & editing.

Jens Blobner - Formal analysis; Investigation; Writing - review & editing.

Sigrid Langer - Data curation; Formal analysis; Investigation; Writing - review & editing.

Nico Teske - Formal analysis; Investigation; Writing - review & editing.

Sertac Dede - Formal analysis; Investigation; Writing - review & editing.

Tao Xu - Formal analysis; Investigation; Writing - review & editing.

Niklas Thon - Formal analysis; Investigation; Writing - review & editing.

Hellen Ishikawa-Ankerhold - Formal analysis; Investigation; Methodology; Resources; Writing - review & editing.

Andreas Straube - Formal analysis; Investigation; Methodology; Resources; Writing - review & editing.

Joerg-Christian Tonn - Formal analysis; Investigation; Methodology; Resources; Writing - review & editing.

Louisa von Baumgarten - Conceptualization; Formal analysis; Funding acquisition; Investigation; Methodology; Project administration; Resources; Supervision; Visualization; Roles/Writing - original draft; Writing - review & editing.

Supplementary materials

Supplementary material associated with this article can be found, in the online version, at doi:10.1016/j.neo.2021.09.001.

References

[1] Achrol AS, Rennert RC, Anders C, Soffietti R, Ahluwalia MS, Nayak L, Peters S, Arvold ND, Harsh GR, Steeg PS, et al. Brain metastases. *Nat Rev Dis Primers* 2019;**5**:5. doi:10.1038/s41572-018-0055-y.

[2] Hellmann MD, Sakai H, Paz-Ares L, Bernabe Caro R, Zurawski B, Kim SW, Carcereny Costa E, Park K, Alexandru A, Lupinacci L, et al. Nivolumab plus ipilimumab in advanced non-small-cell lung cancer. *N Engl J Med* 2019;**381**:2020–31. doi:10.1056/NEJMoa1910231.

[3] Goldberg SB, Schalper KA, Gettinger SN, Mahajan A, Herbst RS, Chiang AC, Lilenbaum R, Wilson FH, Omay SB, Yu JB, Jilaveanu L, Tran T, Pavlik K, Rowen E, Gerrish H, Komlo A, Gupta R, Wyatt H, Ribeiro M, Kluger Y, Zhou G, Wei W, Chiang VL, Kluger HM. Pembrolizumab for management of patients with NSCLC and brain metastases: long-term results and biomarker analysis from a non-randomised, open-label, phase 2 trial. Lancet Oncol. 2020 May;21(5):655-663. doi: 10.1016/S1470-2045(20)30111-X. Epub 2020 Apr 3. PMID: 32251621; PMCID: PMC7380514.

[4] Soffietti R, Abacioglu U, Baumert B, Combs SE, Kinhult S, Kros JM, Marosi C, Metellus P, Radbruch A, Villa Freixa SS, et al. Diagnosis and treatment of brain metastases from solid tumors: guidelines from the European Association of Neuro-Oncology (EANO). *Neuro Oncol* 2017;**19**:162–74. doi:10.1093/neuonc/now241.

[5] You H, Baluszek S, Kaminska B. Supportive roles of brain macrophages in CNS metastases and assessment of new approaches targeting their functions. *Theranostics* 2020;**10**:2949–64. doi:10.7150/thno.40783.

[6] Kudo Y, Haymaker C, Zhang J, Reuben A, Duose DY, Fujimoto J, Roy-Chowdhuri S, Solis Soto LM, Dejima H, Parra ER, et al. Suppressed immune microenvironment and repertoire in brain metastases from patients with resected non-small-cell lung cancer. *Ann Oncol* 2019;**30**:1521–30. doi:10.1093/annonc/mdz207.

[7] Hollmén M, Karaman S, Schwager S, Lisibach A, Christiansen AJ, Maksimow M, Varga Z, Jalkanen S, Detmar M. G-CSF regulates macrophage phenotype and associates with poor overall survival in human triple-negative breast cancer. *Oncoimmunology* 2016;**5**:e1115177. doi:10.1080/2162402x.2015.1115177.

[8] Griesmann H, Drexel C, Milosevic N, Sipos B, Rosendahl J, Gress TM, Michl P. Pharmacological macrophage inhibition decreases metastasis formation in a genetic model of pancreatic cancer. *Gut* 2017;**66**:1278–85. doi:10.1136/gutjnl-2015-310049.

[9] Pyonteck SM, Akkari L, Schuhmacher AJ, Bowman RL, Sevenich L, Quail DF, Olson OC, Quick ML, Huse JT, Teijeiro V, et al. CSF-1R inhibition alters macrophage polarization and blocks glioma progression. *Nat Med* 2013;**19**:1264–72. doi:10.1038/nm.3337.

[10] Maximov V, Chen Z, Wei Y, Robinson MH, Herting CJ, Shanmugam NS, Rudneva VA, Goldsmith KC, MacDonald TJ, Northcott PA, et al. Tumour-associated macrophages exhibit anti-tumoural properties in Sonic Hedgehog medulloblastoma. *Nat Commun* 2019;**10**:2410. doi:10.1038/s41467-019-10458-9.

[11] Cruz-Munoz W, Man S, Xu P, Kerbel RS. Development of a preclinical model of spontaneous human melanoma central nervous system metastasis. *Cancer Res* 2008;**68**:4500–5. doi:10.1158/0008-5472.Can-08-0041.

[12] Francia G, Cruz-Munoz W, Man S, Xu P, Kerbel RS. Mouse models of advanced spontaneous metastasis for experimental therapeutics. *Nat Rev Cancer* 2011;**11**:135–41. doi:10.1038/nrc3001.

[13] Schulz M, Salamero-Boix A, Niesel K, Alekseeva T, Sevenich L. Microenvironmental regulation of tumor progression and therapeutic response in brain metastasis. *Front Immunol* 2019;**10**:1713. doi:10.3389/fimmu.2019.01713.

[14] Travaglini KJ, Nabhan AN, Penland L, Sinha R, Gillich A, Sit RV, Chang S, Conley SD, Mori Y, Seita J, et al. A molecular cell atlas of the human lung from single-cell RNA sequencing. *Nature* 2020;**587**:619–25. doi:10.1038/s41586-020-2922-4.

[15] Wolf Y, Yona S, Kim KW, Jung SMicroglia. seen from the CX3CR1 angle. *Front Cell Neurosci* 2013;**7**:26. doi:10.3389/fncel.2013.00026.

[16] Korbecki J, Simińska D, Kojder K, Grochans S, Gutowska I, Chlubek D, Baranowska-Bosiacka I. Fractalkine/CX3CL1 in Neoplastic Processes. *Int J Mol Sci* 2020;**21**. doi:10.3390/ijms21103723.

[17] Li W, Nava RG, Bribriesco AC, Zinselmeyer BH, Spahn JH, Gelman AE, Krupnick AS, Miller MJ, Kreisel D. Intravital 2-photon imaging of leukocyte trafficking in beating heart. *J Clin Invest* 2012;**122**:2499–508. doi:10.1172/jci62970.

[18] Feng X, Szulzewsky F, Yerevanian A, Chen Z, Heinzmann D, Rasmussen RD, Alvarez-Garcia V, Kim Y, Wang B, Tamagno I, et al. Loss of CX3CR1 increases accumulation of inflammatory monocytes and promotes gliomagenesis. *Oncotarget* 2015;**6**:15077–94. doi:10.18632/oncotarget.3730.

[19] Mulazzani M, Fräßle SP, von Mücke-Heim I, Langer S, Zhou X, Ishikawa-Ankerhold H, Leube J, Zhang W, Dötsch S, Svec M, et al. Long-term in vivo microscopy of CAR T cell dynamics during eradication of CNS lymphoma in mice. *Proc Natl Acad Sci U S A* 2019;**116**:24275–84. doi:10.1073/pnas.1903854116.

[20] Winkler F, Kienast Y, Fuhrmann M, Von Baumgarten L, Burgold S, Mitteregger G, Kretzschmar H, Herms J. Imaging glioma cell invasion in vivo reveals mechanisms of dissemination and peritumoral angiogenesis. *Glia* 2009;**57**:1306–15. doi:10.1002/glia.20850.

[21] Kienast Y, von Baumgarten L, Fuhrmann M, Klinkert WE, Goldbrunner R, Herms J, Winkler F. Real-time imaging reveals the single steps of brain metastasis formation. *Nat Med* 2010;**16**:116–22. doi:10.1038/nm.2072.

[22] Liu Z, Wang Y, Kabraji S, Xie S, Pan P, Liu Z, Ni J, Zhao JJ. Improving orthotopic mouse models of patient-derived breast cancer brain metastases by a modified intracarotid injection method. *Sci Rep* 2019;**9**:622. doi:10.1038/s41598-018-36874-3.

[23] Chen Z, Ross JL, Hambardzumyan D. Intravital 2-photon imaging reveals distinct morphology and infiltrative properties of glioblastoma-associated macrophages. *Proc Natl Acad Sci U S A* 2019;**116**:14254–9. doi:10.1073/pnas.1902366116.

[24] Hambardzumyan D, Gutmann DH, Kettenmann H. The role of microglia and macrophages in glioma maintenance and progression. *Nat Neurosci* 2016;**19**:20–7. doi:10.1038/nn.4185.

[25] Schulz M, Michels B, Niesel K, Stein S, Farin H, Rödel F, Sevenich L, et al. Cellular and molecular changes of brain metastases-associated myeloid cells during disease progression and therapeutic response. *iScience* 2020;**23**:101178. doi:10.1016/j.isci.2020.101178.

[26] Zhang F, Parayath NN, Ene CI, Stephan SB, Koehne AL, Coon ME, Holland EC, Stephan MT, et al. Genetic programming of macrophages to perform anti-tumor functions using targeted mRNA nanocarriers. *Nat Commun* 2019;**10**:3974. doi:10.1038/s41467-019-11911-5.

[27] Murray PJ, Allen JE, Biswas SK, Fisher EA, Gilroy DW, Goerdt S, Gordon S, Hamilton JA, Ivashkiv LB, Lawrence T, et al. Macrophage activation and polarization: nomenclature and experimental guidelines. *Immunity* 2014;**41**:14–20. doi:10.1016/j.immuni.2014.06.008.

[28] Jurga AM, Paleczna M, Kuter KZ. Overview of general and discriminating markers of differential microglia phenotypes. *Front Cell Neurosci* 2020;**14**:198. doi:10.3389/fncel.2020.00198.

[29] Hutter G, Theruvath J, Graef CM, Zhang M, Schoen MK, Manz EM, Bennett ML, Olson A, Azad TD, Sinha R, et al. Microglia are effector cells of CD47-SIRPα antiphagocytic axis disruption against glioblastoma. *Proc Natl Acad Sci U S A* 2019;**116**:997–1006. doi:10.1073/pnas.1721434116.

[30] von Roemeling CA, Wang Y, Qie Y, Yuan H, Zhao H, Liu X, Yang Z, Yang M, Deng W, Bruno KA, et al. Therapeutic modulation of phagocytosis in glioblastoma can activate both innate and adaptive antitumour immunity. *Nat Commun* 2020;**11**:1508. doi:10.1038/s41467-020-15129-8.

[31] Qiao S, Qian Y, Xu G, Luo Q, Zhang Z. Long-term characterization of activated microglia/macrophages facilitating the development of experimental brain metastasis through intravital microscopic imaging. *J Neuroinflammation* 2019;**16**:4. doi:10.1186/s12974-018-1389-9.

[32] Zhang M, Hutter G, Kahn SA, Azad TD, Gholamin S, Xu CY, Liu J, Achrol AS, Richard C, Sommerkamp P, et al. Anti-CD47 treatment stimulates phagocytosis of glioblastoma by M1 and M2 polarized macrophages and promotes m1 polarized macrophages in vivo. *PLoS One* 2016;**11**:e0153550. doi:10.1371/journal.pone.0153550.

[33] Shen F, Zhang Y, Jernigan DL, Feng X, Yan J, Garcia FU, Meucci O, Salvino JM, Fatatis A. Novel small-molecule CX3CR1 antagonist impairs metastatic seeding and colonization of breast cancer cells. *Mol Cancer Res* 2016;**14**:518–27. doi:10.1158/1541-7786.Mcr-16-0013.

[34] Liu C, Luo D, Streit WJ, Harrison JK. CX3CL1 and CX3CR1 in the GL261 murine model of glioma: CX3CR1 deficiency does not impact tumor growth or infiltration of microglia and lymphocytes. *J Neuroimmunol* 2008;**198**:98–105. doi:10.1016/j.jneuroim.2008.04.016.

[35] Hulshof S, van Haastert ES, Kuipers HF, van den Elsen PJ, De Groot CJ, van der Valk P, Ravid R, Biber K. CX3CL1 and CX3CR1 expression in human brain tissue: noninflammatory control versus multiple sclerosis. *J Neuropathol Exp Neurol* 2003;**62**:899–907. doi:10.1093/jnen/62.9.899.

[36] Karschnia P, Scheuer C, Heß A, Später T, Menger MD, Laschke MW. Erythropoietin promotes network formation of transplanted adipose tissue-derived microvascular fragments. *Eur Cell Mater* 2018;**35**:268–80. doi:10.22203/eCM.v035a19.

[37] Tei N, Tanaka J, Sugimoto K, Nishihara T, Nishioka R, Takahashi H, Yano H, Matsumoto S, Ohue S, Watanabe H, et al. Expression of MCP-1 and fractalkine on endothelial cells and astrocytes may contribute to the invasion and migration of brain macrophages in ischemic rat brain lesions. *J Neurosci Res* 2013;**91**:681–93. doi:10.1002/jnr.23202.

[38] Käufer C, Chhatbar C, Bröer S, Waltl I, Ghita L, Gerhauser I, Kalinke U, Löscher W. Chemokine receptors CCR2 and CX3CR1 regulate viral encephalitis-induced hippocampal damage but not seizures. *Proc Natl Acad Sci U S A* 2018;**115**:E8929–38. doi:10.1073/pnas.1806754115.

[39] Curtaz CJ, Schmitt C, Herbert SL, Feldheim J, Schlegel N, Gosselet F, Hagemann C, Roewer N, Meybohm P, Wöckel A, et al. Serum-derived factors of breast cancer patients with brain metastases alter permeability of a human blood-brain barrier model. *Fluids Barriers CNS* 2020;**17**:31. doi:10.1186/s12987-020-00192-6.

[40] Swierczak A, Cook AD, Lenzo JC, Restall CM, Doherty JP, Anderson RL, Hamilton JA. The promotion of breast cancer metastasis caused by inhibition of CSF-1R/CSF-1 signaling is blocked by targeting the G-CSF receptor. *Cancer Immunol Res* 2014;**2**:765–76. doi:10.1158/2326-6066.Cir-13-0190.

[41] Zhou X, Mulazzani M, von Mücke-Heim IA, Langer S, Zhang W, Ishikawa-Ankerhold H, Dreyling M, Straube A, von Baumgarten L. The role of BAFF-R signaling in the growth of primary central nervous system lymphoma. *Front Oncol* 2020;**10**:682. doi:10.3389/fonc.2020.00682.

[42] von Baumgarten L, Brucker D, Tirniceru A, Kienast Y, Grau S, Burgold S, Herms J, Winkler F. Bevacizumab has differential and dose-dependent effects on glioma blood vessels and tumor cells. *Clin Cancer Res* 2011;**17**:6192–205. doi:10.1158/1078-0432.Ccr-10-1868.

[43] Winkler F. The brain metastatic niche. *J Mol Med (Berl)* 2015;**93**:1213–20. doi:10.1007/s00109-015-1357-0.

[44] Berghoff AS, Liao Y, Karreman MA, Ilhan-Mutlu A, Gunkel K, Sprick MR, Eisen C, Kessler T, Osswald M, Wünsche S, et al. Identification and characterization of cancer cells that initiate metastases to the brain and other organs. *Mol Cancer Res* 2021;**19**:688–701. doi:10.1158/1541-7786.Mcr-20-0863.

[45] Berghoff AS, Rajky O, Winkler F, Bartsch R, Furtner J, Hainfellner JA, Goodman SL, Weller M, Schittenhelm J, Preusser M. Invasion patterns in brain metastases of solid cancers. *Neuro Oncol* 2013;**15**:1664–72. doi:10.1093/neuonc/not112.

[46] Villa A, Gelosa P, Castiglioni L, Cimino M, Rizzi N, Pepe G, Lolli F, Marcello E, Sironi L, Vegeto E, et al. Sex-Specific Features of Microglia from Adult Mice. *Cell Rep* 2018;**23**:3501–11. doi:10.1016/j.celrep.2018.05.048.

[47] Holtmaat A, Bonhoeffer T, Chow DK, Chuckowree J, De Paola V, Hofer SB, Hübener M, Keck T, Knott G, Lee WC, et al. Long-term, high-resolution

imaging in the mouse neocortex through a chronic cranial window. *Nat Protoc* 2009;**4**:1128–44. doi:10.1038/nprot.2009.89.

[48] Goldey GJ, Roumis DK, Glickfeld LL, Kerlin AM, Reid RC, Bonin V, Schafer DP, Andermann ML. Removable cranial windows for long-term imaging in awake mice. *Nat Protoc* 2014;**9**:2515–38. doi:10.1038/nprot.2014.165.

[49] Gyoneva S, Hosur R, Gosselin D, Zhang B, Ouyang Z, Cotleur AC, Peterson M, Allaire N, Challa R, Cullen P, et al. Cx3cr1-deficient microglia exhibit a premature aging transcriptome. *Life Sci Alliance* 2019;**2**. doi:10.26508/lsa.201900453.